Supplementary Information

for

Large-Area Epitaxial Monolayer MoS_2

Dumitru Dumcenco[1†], Dmitry Ovchinnikov[1†], Kolyo Marinov[1†], Predrag Lazić[2], Marco Gibertini[3], Nicola Marzari[3], Oriol Lopez Sanchez[1], Yen-Cheng Kung[1], Daria Krasnozhon[1], Ming-Wei Chen[1], Simone Bertolazzi[1], Philippe Gillet[4], Anna Fontcuberta i Morral[3], Aleksandra Radenovic[5], Andras Kis[1*]

[1]*Electrical Engineering Institute, Ecole Polytechnique Federale de Lausanne (EPFL), CH-1015 Lausanne, Switzerland*
[2]*Institute Ruđer Bošković (IRB), HR-10000 Zagreb, Croatia*
[3]*Institute of Materials, Ecole Polytechnique Federale de Lausanne (EPFL), CH-1015 Lausanne, Switzerland*
[4]*Institute of Condensed Matter Physics, Ecole Polytechnique Federale de Lausanne (EPFL), CH-1015 Lausanne, Switzerland*
[5]*Institute of Bioengineering, Ecole Polytechnique Federale de Lausanne (EPFL), CH-1015 Lausanne, Switzerland*

[†]*These authors contributed equally*
[*]*Correspondence should be addressed to: Andras Kis, andras.kis@epfl.ch*

1. Substrate preparation

The preparation of atomically smooth terraces on the sapphire surface is critical to achieving control over lattice orientation during CVD growth.

We start with commercially available EPI grade polished c-plane sapphire (University Wafers) which is first diced into 1 cm × 1 cm dies. An AFM image of the as-received substrate with the corresponding height histogram from a 500 nm × 500 nm area is shown on Figure S1a. The surface is relatively smooth, with the height histogram showing a standard deviation σ = 154 pm, lower than for typical SiO_2 surfaces (σ ~ 300 pm). The sapphire dies are loaded in a quartz tube and annealed in a tube furnace in air for 1h at 1000 °C prior to the growth run. Following the annealing procedure, the samples are allowed to cool to room temperature in air before we place them in the CVD growth furnace. An AFM image of the surface after annealing is shown on Figure S1b and demonstrates the dramatic change in surface morphology during annealing. The resulting surface shows atomically flat surfaces with atomic steps due to the small miscut induced during the cutting of the sapphire boule. Based on the height histogram, we extract a step size ~ 2.1 Å and a terrace width ~ 70 nm. Terraces are atomically smooth, with a surface roughness σ = 33 pm. This height variation is smaller than the diameters of oxygen, aluminum or sulphur atoms (122 pm, 242 pm and 205 pm respectively). Such atomically smooth surfaces allow the van der Waals interaction between sapphire and MoS_2 to control the lattice orientation during the CVD growth of monolayer MoS_2.

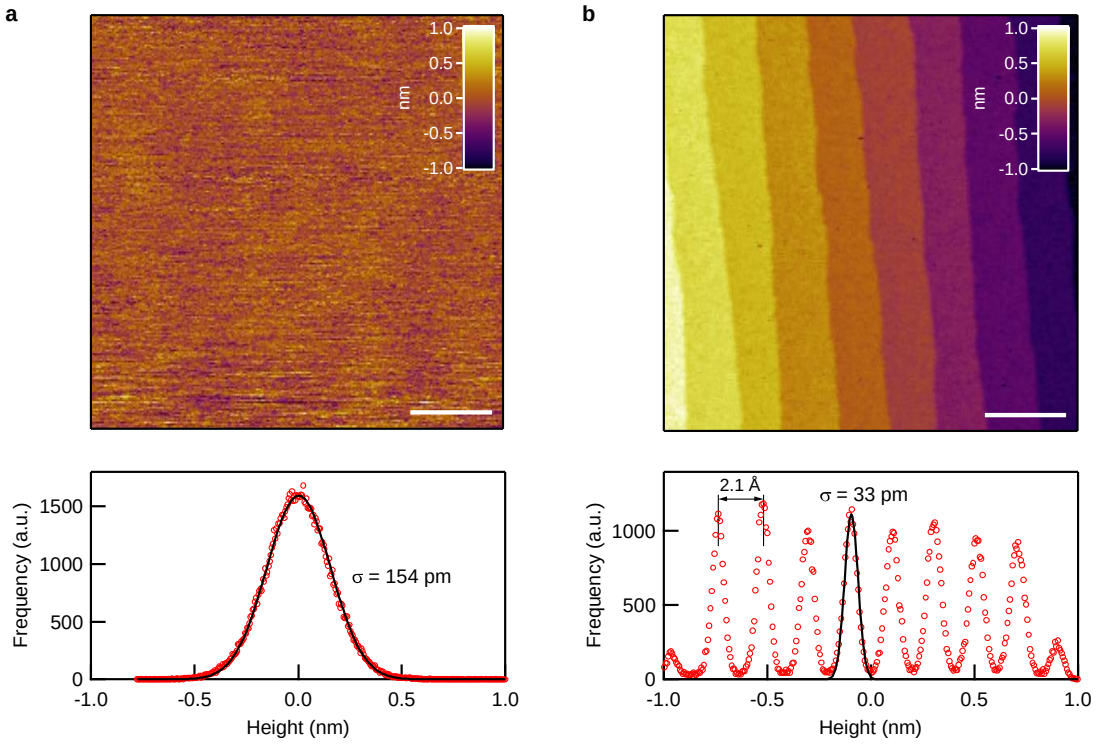

Figure S1. Effect of annealing in air on the morphology of c-plane sapphire. a, AFM image of the as received sapphire surface. Top panel: AFM image. Bottom panel: height histogram with a Gaussian fit showing a standard deviation σ = 154 pm. **b**, AFM image of annealed sapphire used here as the growth substrate. After annealing in air, the surface shows atomically smooth terraces. Top panel: AFM image. Bottom panel: height histogram with a Gaussian fit showing a standard deviation σ = 33 pm and a terrace height ~ 2.1 Å. The color scales in **a** and **b** are the same (2 nm). The scale bars are 100 nm long.

The importance of surface annealing can also be seen on Figure S2 where we show an optical image and orientation histogram for CVD MoS_2 on a sapphire sample which was not annealed. Using a surface without the annealing treatment results in a wide distribution of single crystal orientations (Figure S2a), as seen on the associated orientation histogram (Figure S2b). A relatively large number of particles, presumably growth seeds can also be seen.

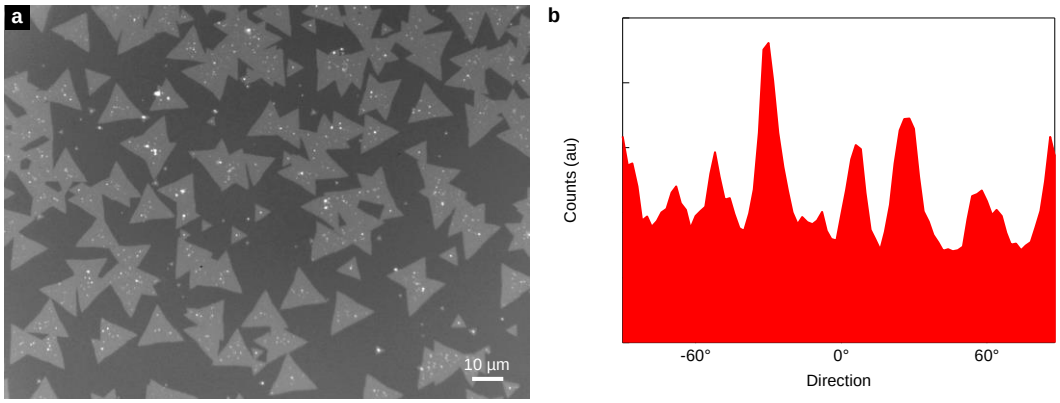

Figure S2. Effect of sapphire surface annealing on the lattice orientation of CVD-grown MoS_2. a, Optical image of a triangular MoS_2 single crystals grown on sapphire without annealing. **b,** Orientation histogram obtained from the optical image in **a**.

2. Growth setup

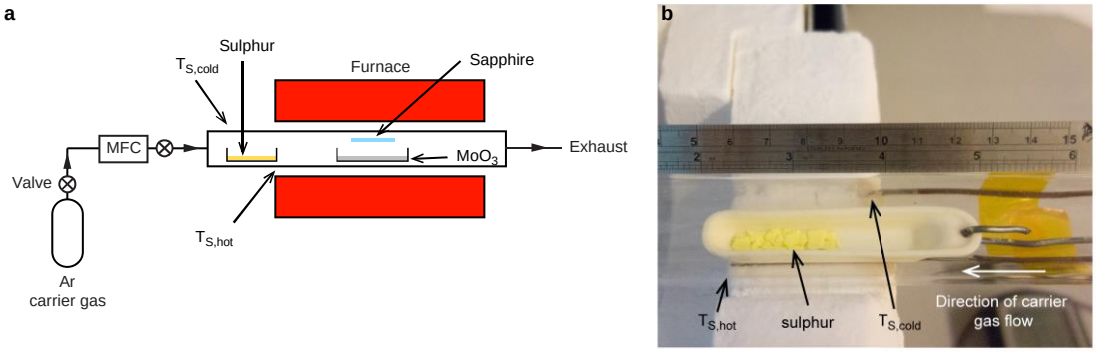

Figure S3. Schematic of the growth system a, Schematic drawing of the growth system. **b,** Sulphur pieces are loaded in an alumina boat placed at the end of the heated section of the split-tube three zone furnace. All three zones of the furnace are maintained at the same temperature. The boat stays in the same place during the entire growth run. The temperature at the two different points $T_{S,hot}$ and $T_{S,cold}$ is measured using a thermocouple.

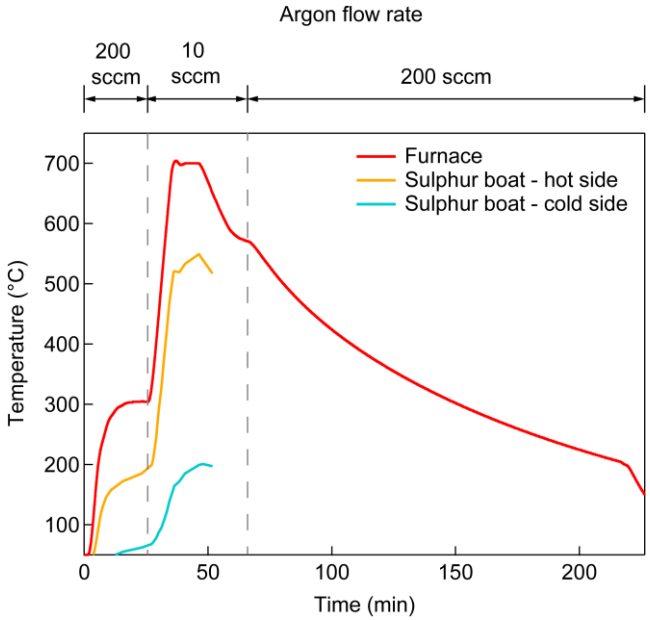

Figure S4. Time dependence of growth parameters. Temperature and argon carrier gas flow rate as a function of time. The system is maintained at atmospheric pressure during the entire growth run.

3. SAED analysis

To further investigate the relative crystalline orientations of triangles on a large scale, the alignment of their diffraction pattern has been used. The alignment of triangles on the macro scale is clearly visible optically (Figure 1b,c) and confirmed by the orientation histogram (Figure 1f). Using select-area electron diffraction (SAED), we perform a more precise determination of triangle alignment by probing the changes of diffraction patterns and related lattice rotations of different triangles. Multiple SAED patterns have been recorded from different locations on the sample. A low-resolution TEM (LR-TEM) micrograph (Figure S5a) and related representative SAED patterns (Figure S5 b-e) are presented on Figure S5. The diffraction pattern alignment of two pairs of triangles (1-3 and 2-4) is evident. Moreover, red lines in parts b-e are parallel, indicating that these triangles have the same lattice orientation.

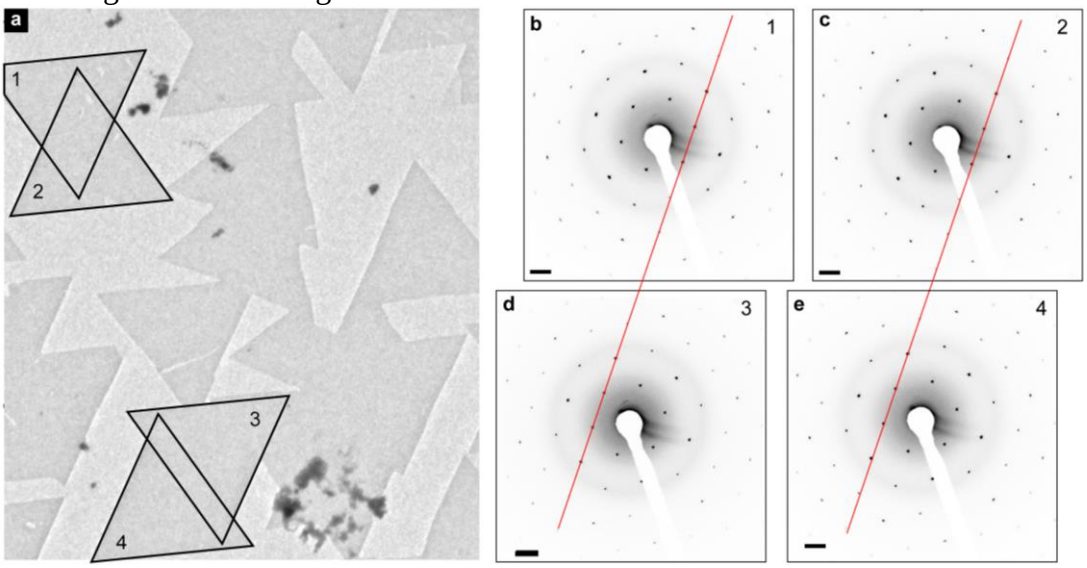

Figure S5. SAED study of crystalline orientations of CVD MoS_2. a, LR-TEM micrograph of several merging triangles. Scale bar - 5 µm. Two pairs of selected triangles are highlighted. **b-e,** SAED diffraction patterns acquired on triangles labeled 1-4 in part a. Scale bar: 2 nm^{-1}. Parallel red lines are provided as a guide for tracking the relative orientations of diffraction patterns.

Furthermore, we have performed measurements on several triangles to precisely identify the orientation of the crystalline lattice with respect to the triangle orientation. The key to identifying these orientations is the comparison of intensities of the first family of diffraction spots [-1100].[1] The lattice of MoS_2 consists of two sublattices - Mo and S, which results in small differences of intensities in the [-1100] family of diffraction spots in the single-layer limit because of inversion symmetry breaking, as confirmed previously experimentally by correlation between diffraction patterns and HR-TEM micrographs, as well as by modeling.[1, 2] Lower-intensity diffraction correspond to the sulfur sublattice.[2]

Figure S6 presents merged triangles rotated by 180° with respect to each other. On Figure S6a a micrograph showing merged triangles with the opposite geometrical orientation is presented. We mark the triangles Triangle 1 and Triangle 2 and further inspect each triangle separately using SAED.

Figure S6b presents the SAED pattern of Triangle 1. Furthermore, we analyze the intensities in the [-1100] diffraction spot family. To illustrate the relationship between the intensities of diffraction spots inside the [-1100] family, we plot the profile along the red line, with the corresponding intensities plotted on part Figure S6d. The same

analysis for Triangle 2 is shown on Figures S6c and e. We mark with blue and red the spots corresponding to the Mo and S sublattices. We find that the lattices in the two triangles are also rotated by 180°. All the triangles we examined showed the same asymmetry in SAED spot intensities, indicating that same relationship between triangle edge and lattice orientation, shown on Figure S6a.

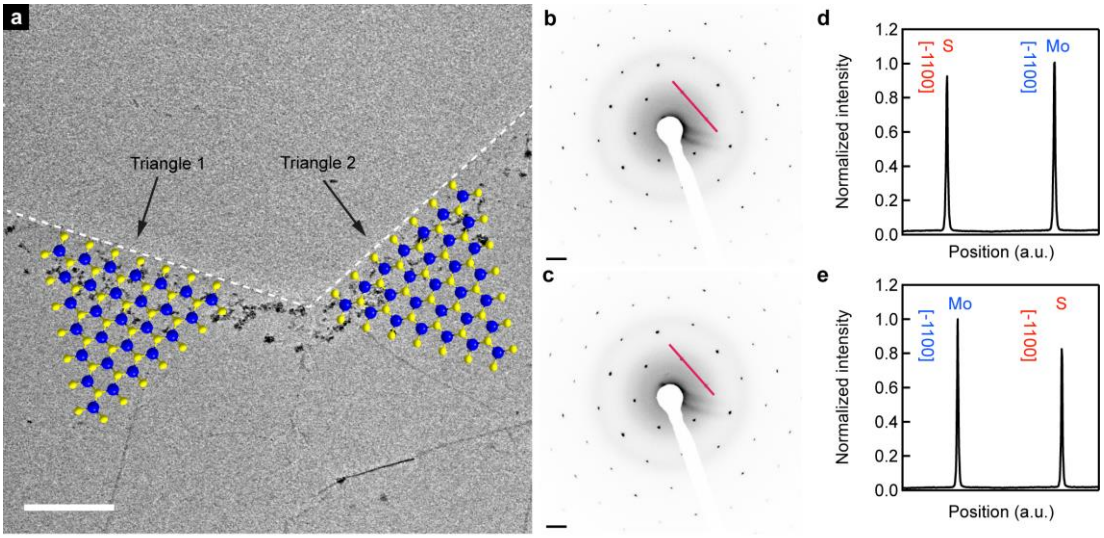

Figure S6. SAED study of crystalline orientations of CVD MoS_2. a, TEM micrograph of two merging triangles of CVD MoS_2 rotated by 180°. The overlaid structural model is for illustration only. Scale bar - 0.5 µm. **b,** SAED pattern acquired on Triangle 1. Scale bar 2 nm^{-1}. **c,** Same as b but for Triangle 2. Scale bar - 2 nm^{-1}. **d,** Diffraction spot intensity plotted along the red line in **b** for Triangle 1. **e,** Diffraction spot intensity plotted along the red line in **c** for Triangle 2.

4. Calculations of the sapphire-MoS_2 van der Waals interaction

In order to perform first-principles simulations of MoS_2 on the surface of Al_2O_3 within periodic boundary conditions, we need to define a supercell (the coincident site lattice) that can accommodate both lattices, allowing for a relative rotation between them by an angle θ, and possibly for some small strain in the monolayer. This corresponds to assuming that van der Waals interactions are sufficiently strong to enforce commensurability between MoS_2 and the underlying sapphire surface. We start from the unit cells of the MoS_2 and sapphire, shown in Figure S7.

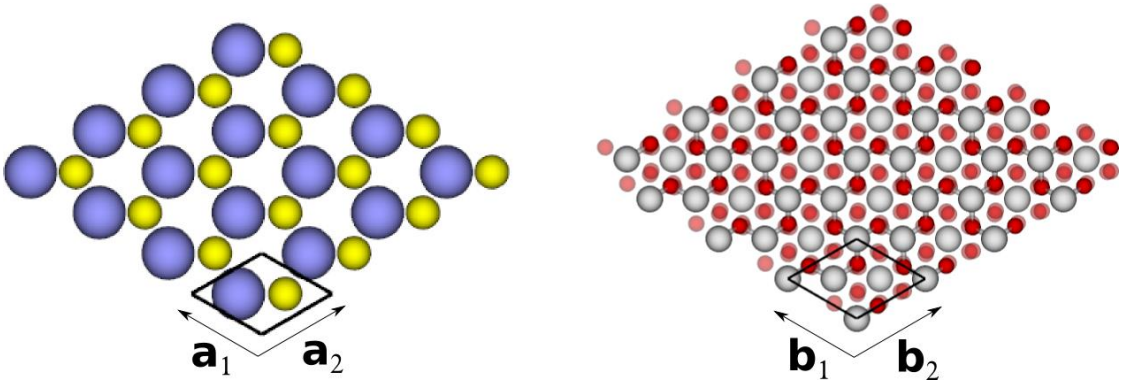

Figure S7. Unit cells of single-layer MoS_2 (left) and 5-layers Al_2O_3 sapphire (right).

Since both lattices are hexagonal, the supercell will also be hexagonal with a primitive lattice vector $\boldsymbol{C}$ that can be written as

$$\boldsymbol{C} = n_1\,\boldsymbol{a}_1 + n_2\,\boldsymbol{a}_2 = (1+\epsilon)\,R_\theta(m_1\,\boldsymbol{b}_1 + m_2\,\boldsymbol{b}_2). \quad (1)$$

Here $\boldsymbol{a}_1, \boldsymbol{a}_2$ and $\boldsymbol{b}_1, \boldsymbol{b}_2$ are the primitive lattice vectors of the sapphire surface and MoS_2 respectively, n_1, n_2 and m_1, m_2 are integers, and R_θ and ϵ are the rotation and strain to be applied to MoS_2. The size L=|$\boldsymbol{C}$| of the supercell can thus assume only discrete values, and each supercell is identified by a set of integers $(n_1, n_2; m_1, m_2)$ for which there always exists a couple (θ, ϵ) so that Eq. (1) is satisfied.

In Figure S8. we consider for instance a supercell identified by (2,1;3,1). This corresponds in Wood's notation[3] to a $\sqrt{3} \times \sqrt{3}\,R\,30°$ supercell for sapphire and a $\sqrt{7} \times \sqrt{7}\,R\,19.11°$ supercell for MoS_2. The supercell size is L = 8.34 Å and in order to satisfy Eq. (1) we need to strain the MoS_2 lattice by 1.9% (ε = 0.019) and to introduce a relative rotation by $\theta \simeq 10.89°$ between sapphire and MoS_2. In Figure S8. we report the relative rotation angle θ as a function of size L for all possible supercells for which the strain we need to apply to MoS_2 (represented by the color coding) is smaller than 5%. For simplicity we considered only angles $0° < \theta < 60°$, since any other angle corresponds either to the same structure by symmetry or to a structure obtained by applying inversion to MoS_2.

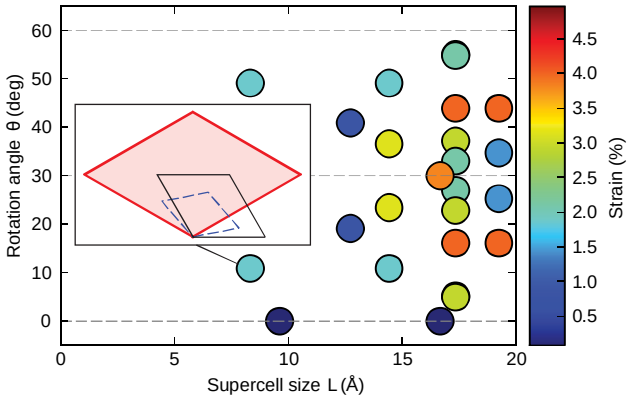

Figure S8. Graphical representation of possible supercells for MoS_2 on sapphire. Each circle denotes a supercell, characterized by its size L, the relative rotation angle θ, and the strain which has to be applied to MoS_2 in order to fulfill Eq. (1) and here represented by the color coding. The inset shows an example of supercell (red shaded area) corresponding to the set of integers (2,1;3,1) (see text). In this case an angle $\theta \simeq 10.89°$ is present between the primitive cell of MoS_2 (blue dashed line) and that of the sapphire surface (black solid line).

In addition to the relative orientation of the unit cells, there is an additional degree of freedom related to the relative shift between the MoS_2 and sapphire lattices. To determine influence of that factor we have generated 3 nonequivalent MoS_2 layer positions for one relative orientation of the unit cells (the 0 orientation). Representative examples of cells used for calculation are shown in Figure S9.

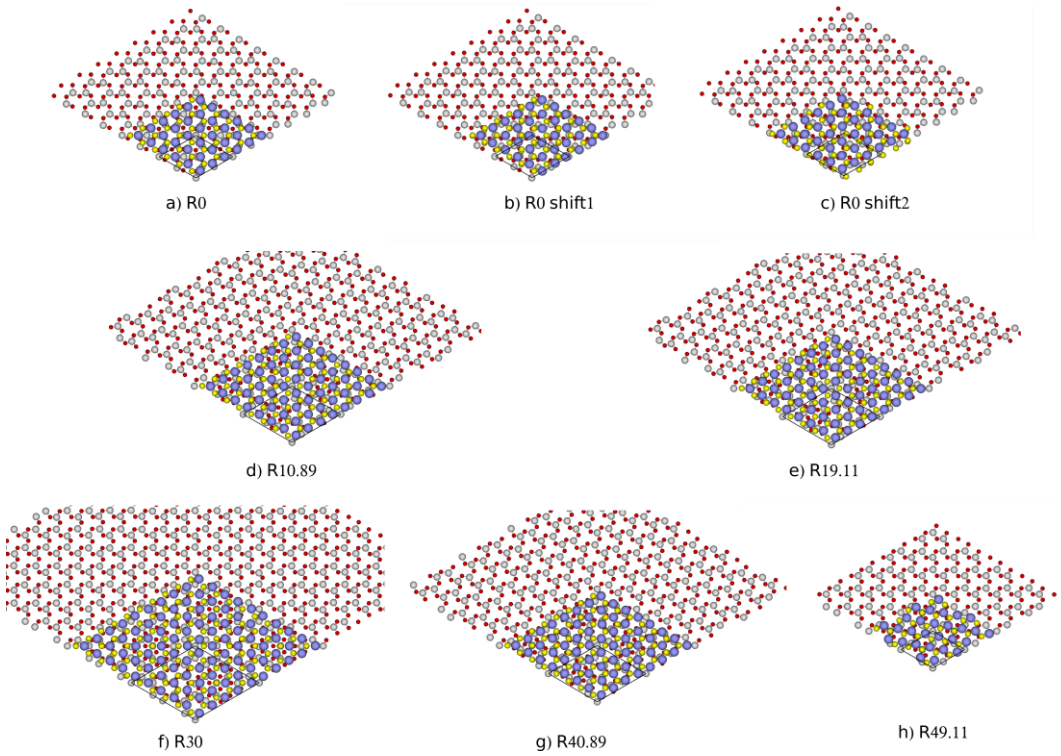

Figure S9. Representative examples of generated common supercells. Rotation angle of MoS_2 unit cell is given as x (in Rx). MoS_2 is shown only partially covering the surface so that underlying Al_2O_3 structure is visible as well (only the last layer is shown). For the R0 cell, three different relative positions of MoS_2 with respect to sapphire are shown.

The main results of binding energies between MoS_2 and Al_2O_3 are given in Table 1. for the five smallest supercells with a strain smaller than 5%, together with the corresponding values of L, θ, and ϵ. Results are also reported for the smallest supercell with $\theta = 30°$. The binding energy is defined as the energy difference between the relaxed system and the system parts - i.e. calculations of the self-standing MoS_2 slab are done with the strained slab. The influence of strain is discussed further in the text.

We also compared two different codes and functionals: the PWscf code of the Quantum-ESPRESSO distribution[4] with a revised version[5] of the non-local density functional by Vydrov and Van Voorhis[6] (rVV10) and VASP,[7,8] using PAW datasets[9, 10] and vdW-DF[11,12, 13] with opt88.

We present here the results obtained using the Quantum-ESPRESSO code; results for VASP are closely similar. The binding energies for the five smallest supercells with a strain smaller that 5% are given in Table 1, together with the corresponding values of L, θ, and ϵ. Results are also reported for two supercells with $\theta = 30°$.

		Supercell					
Supercell size L		8.34 Å	8.34 Å	9.63 Å	12.74 Å	12.74 Å	16.68 Å
Rotation angle θ		49.11°	10.89°	0°	19.11°	40.89°	30°
Strain ϵ		1.9%	1.9%	0.1%	0.9%	0.9%	3.8%
Binding Energy (meV/MoS_2 Unit)	Al	−256 (−290)	−256 (−290)	−296 (−296)	−285 (−292)	−285 (−292)	−196 (−315)
	OH	−185 (−218)	−184 (−218)	−224 (−224)	−215 (−223)	−214 (−222)	−116 (−236)

Table 1. Geometrical parameters and binding energies (in meV per MoS_2 unit) corresponding to different supercells of MoS_2 on sapphire with Al and OH surface termination. The values in parenthesis are binding energies after subtracting the elastic contribution due to the strain on MoS_2. Supercell sizes and strains have been obtained using the calculated equilibrium lattice constants of the sapphire surface (4.814 Å) and of MoS_2 (3.212 Å). Calculations were performed using the PWscf code of the Quantum-ESPRESSO distribution[4] with a revised version[5] of the non-local density functional by Vydrov and Van Voorhis[6] (rVV10).

First, we note that the binding energy is always negative and, for a given supercell size, does not depend on the rotation angle. Moreover, although the Al surface is more reactive and binds more strongly the MoS_2 layer by almost 70 meV/MoS_2 unit, the relative stability of different supercells is very similar for both surface terminations. In particular, the supercell corresponding to perfectly aligned lattices (i.e. $\theta = 0°$) is the most stable one by approximately 10 meV/MoS_2 unit. Nonetheless, we do not find a subdominant orientation rotated by 30°. The supercell corresponding to $\theta = 30°$ turns out to be unfavourable, although this is mainly due to the large strain that is necessary to apply to MoS_2 in order to have commensurability.

This condition, on the other hand, is not completely justified, as van der Waals interactions typically do not force the epilayer to be exactly commensurate with the substrate. It is thus important to estimate the binding energy in the case of incommensurate growth of MoS_2 on sapphire. To a first approximation, this could be done by subtracting from the binding energies in Table 1 the contribution due to the elastic energy associated with the strain on MoS_2 that we introduced to satisfy the commensurability condition. We stress that values obtained in this way represent upper bounds to the true binding energy. Indeed, in a truly incommensurate situation we would not have the perfect registry between substrate and MoS_2 that we impose in the underlying commensurate calculation. This effect is more significant for highly incommensurate orientations (e.g., $\theta = 30°$) when ϵ is larger. In Table 1, we show in parenthesis the binding energies obtained by using the equation of state of MoS_2 to estimate the elastic contribution. We note that in this case the $\theta = 30°$ orientation is the most stable one by 12 (19) meV/MoS_2 unit for OH (Al) termination. A more conclusive statement on the relative stability between the two is not feasible, owing to a possible overestimation of the binding energy for $\theta = 30°$.

To put binding energies in perspective, we can compare them with the binding energy of graphene layers in bulk graphite, which is of almost pure van der Waals nature and is 50 meV per carbon atom which is equivalent to 0.303 J/m^2. For MoS_2, 296 meV/MoS_2 unit is equivalent to 0.537 J/m^2.

In order to further explore the nature of interaction, we have visualized the charge transfer by calculating the charge density difference between the system and its parts as well as visualizing the nonlocal correlation binding energy which gives rise to van

der Waals interaction. The definition of the nonlocal correlation binding energy is given in ref. 14 while a very recent physical interpretation of the nature of nonlocal correlation binding energy can be found in ref. 15

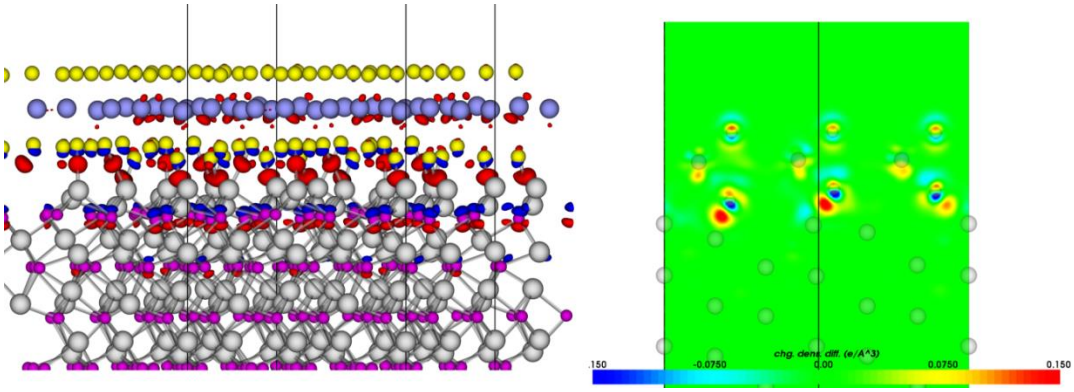

Figure S10. Charge density difference for the R0(a) supercell. Isosurfaces (left) for the values 0.1 (red) and -0.1 e/Å^3 (blue) are shown. Cross-section in the plane along the longer diagonal of the supercell is given. Color code shows values from -0.15 (blue) to 0.15 e/Å^3 (red).

Charge density difference and nonlocal correlation binding energy density are calculated for the R0 system and given in Figures S10 and S11. For visualization of the nonlocal binding energy density we have used the JuNoLo code[16] to recalculate them from the charge densities obtained using VASP.

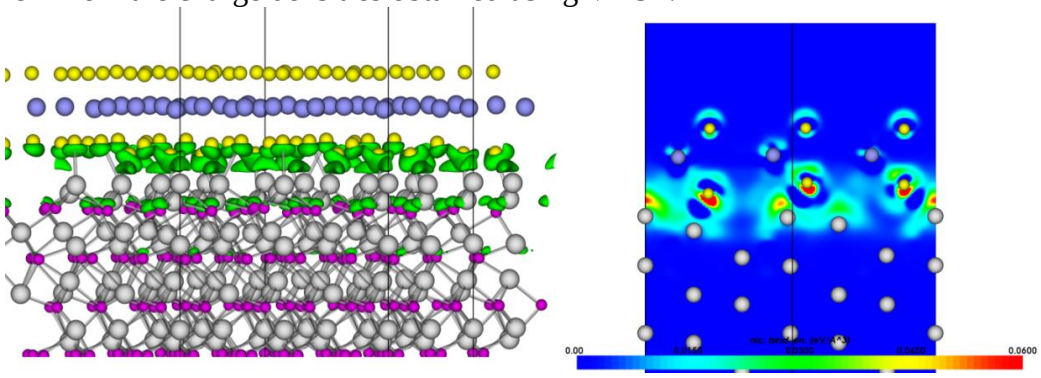

Figure S11. Nonlocal binding energy density - green isosurface (left) for the value 0.04 eV/Å^3 and in-plane cross-section along the longer diagonal of the supercell (left) - values from 0 (blue) to 0.06 eV/Å^3 (red).

The nonlocal binding energy is 10% lower than the total binding energy, implying that all the other contributions are actually repulsive. We can therefore describe this adsorption as being almost exclusively van der Waals in nature (95% contribution), with some chemical modifications which are of repulsive character (5% contribution). Obviously, vdW interactions pull the MoS_2 layer closer to the Al_2O_3 surface gaining energy from nonlocal correlations, achieving optimum at such distances that even some repulsion can be allowed between the fragments. This type of adsorption is rather common and was named *physisorption with chemical modulation*[17] for the case of graphene on Ir(111) or *weak adsorption and strong interaction*[18] for graphene on Ni(111) surface.

However, this particular system shows an even richer adsorption interaction picture than graphene on (111) metal surfaces which we try to elucidate below.

In describing the adsorption mechanism in the case of MoS_2 on Al_2O_3 surface we start from the results in Table 1. By doing naive lattice matching that involves straining the MoS_2 layer, we obtain by far as the best adsorption configuration R30. However, when the strain of the MoS_2 is taken into account so that the adsorption

energy (rather than the binding energy) is calculated, we discover that such a configuration would not even be possible - i.e. in total it would not represent an energy gain and would be unstable. The origin of such large dependence of the binding energy on the MoS_2 strain lies in the source of the nonlocal binding energy (which is almost the complete value of the binding energy). Namely - looking at the nonlocal binding energy shape in Figure S11, we observe blobs formed around alumina and sulfur atoms. Nonlocal interaction energy stems from the interaction between electronic densities in these two regions which can be proven by reducing the nonlocal correlation interaction length, as for example in refs. 16 and 19 but it is beyond the scope of this paper. The important thing to notice is that the amount of this interaction is very sensitive to relative positions of sulfur and alumina atoms and applying a strain on the MoS_2 layer (even a small strain) can cause a very good registry of the S-Al atoms (very regular pattern in which many of the S-Al pairs are very close yielding large amounts of the vdW interaction) giving rise to an unphysically large binding energy. It is not impossible that layered structures such as MoS_2 attain some strain in order to keep a certain registry with the substrate yielding in total the largest adsorption energy. A very nice example is graphene on Ir(111) which grows in a 10×10 over 9×9 Moiré structure, where also a part of the strain in graphene is compensated by its buckling.[20] Modeling such a situation in the MoS_2/Al_2O_3 system is however beyond the scope of this paper.

The main difference between MoS_2 on sapphire as compared to graphene on (111) metallic surfaces is the much smoother electronic structure of the metallic surfaces which makes the system much less sensitive to the exact relative position of the carbon atoms with respect to the underlying metal. With MoS_2 on sapphire, the row (point)-like structure of the Al_2O_3 surface shows large sensitivity to the relative positions of sulfur atoms with respect to the alumina atoms of the surface.

Theoretical calculations based on DFT could in principle determine the best orientation and relative position of the MoS_2 layer structure with more precision if enough CPU power were available to perform calculations for large cells with small strains.

We expect the MoS_2 structure in the experiment to have a very small strain growing in specific orientation with the surface obtaining the largest possible binding energy almost exclusively from the vdW interactions between sulfur-alumina atoms. From the energy differences obtained in our calculations, we conclude that one specific configuration will be dominant and stable at given temperatures, while still keeping relatively small energy barriers between different orientations yielding unlikely growth in the less favorable directions and remaining there due to slow kinetics. The influence of the edges in the finite triangle-shaped structures remains elusive at the moment – however, monolayer structure should determine stability in the thermodynamic limit.

Based on the DFT findings presented above, we decided to make the simplest possible model of van der Waals adsorption for this system. Namely, we simulate adsorption of the MoS_2 monolayer on the sapphire surface by simply calculating only the semi-empirical vdW contributions,[21] based on pairwise atomic interactions:

$$E_{bind} = -\sum_{i,j} \frac{C_6}{r_{ij}^6} \tag{2}$$

We sum over all pairs of bottom sulfur atoms and top alumina atoms since all other contributions are much smaller because of the $1/r^6$ dependence of the vdW force, also indicated by the DFT calculations.

We use the C_6 value of 1 since it is a simple scaling factor and we are only interested in the difference between various configurations. However, for the given adsorption energies per MoS_2 unit in Figure S12 one can perform rescaling by taking the adsorption energy value as obtained from DFT calculations per MoS_2 unit cell as the average value.

This model, however simple - to our surprise, yields results short of spectacular. Namely, it predicts clearly a single orientation and position as the absolutely best one while all the other orientations of the MoS_2 layer relative to the surface - and all corresponding positions - are almost identical in energy. This means that the MoS_2 layer would rotate and slide without any energy penalty until it finds the best possible configuration for adsorption - dictated solely by vdW interactions. We believe that this result is general for all vdW heterostructures and hence we suggest this method as an excellent tool for prediction of such structures.

For calculations, we took an unstrained MoS_2 monolayer with a given relative rotation of the unit cell relative to the sapphire surface. MoS_2 was at an average height from the sapphire surface as obtained from the DFT calculations (3.24 Å from top Al to Mo). In addition, we also tested two other heights, one 0.2 Å above and other 0.2 Å below the selected value. The binding energy is calculated for 1600 relative positions of MoS_2 with respect to the surface. In each calculation at least 2000 sulfur atoms were involved. Results are given in Figure S12.

What is visible from the results in Figure S12 is that almost all orientations and relative positions of the MoS_2 monolayer with respect to the surface have identical binding energies which depend only on the distance between MoS_2 and the surface - getting larger as MoS_2 approaches the surface. However, 0° and 60° orientations are very different from the rest, showing an enormous sensitivity to the exact arrangement of MoS_2 over the sapphire surface and a typical eggbox shape of the potential.

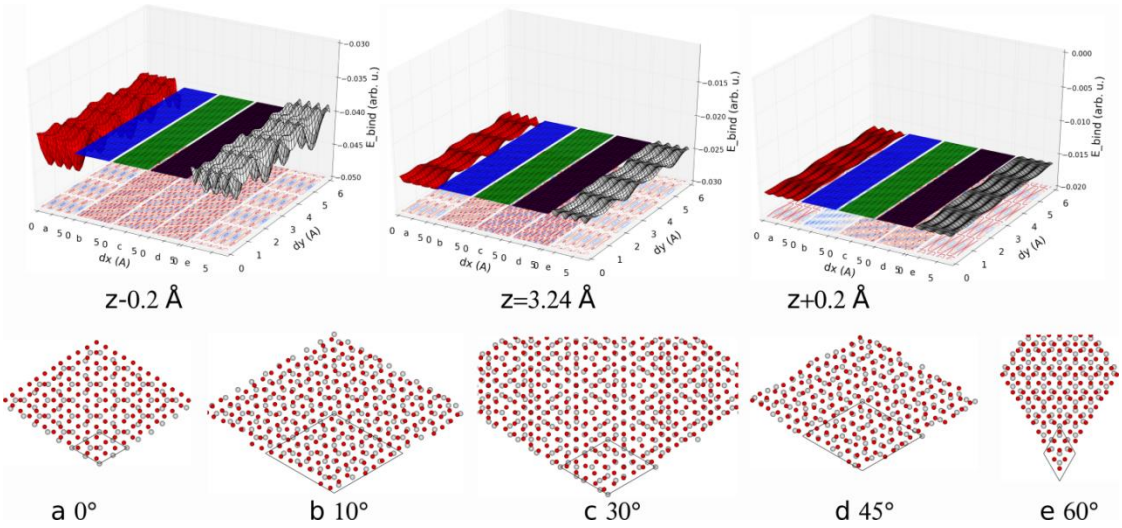

Figure S12. Top row, binding energies for three distances of MoS_2 with respect to the surface. In each plot 5 stripes are given corresponding to appropriate MoS_2 rotations with respect to the sapphire (shown in the second row - only top Al and bottom S atoms are drawn). a-red, b-blue, c-green, d-gray and e-white. Each point on a stripe corresponds to a relative x-y shift of the MoS_2 layer with respect to the sapphire surface (0,0 shown in bottom row). Bottom left corner of each stripe corresponds to dx,dy=(0,0) while top right point is (6 Å,6 Å). Below each stripe the contour plot is also given.

To determine the sensitivity of the eggbox potential on the orientation of the MoS_2 monolayer, we compare results for 0° and 2° rotation in Figure S13.

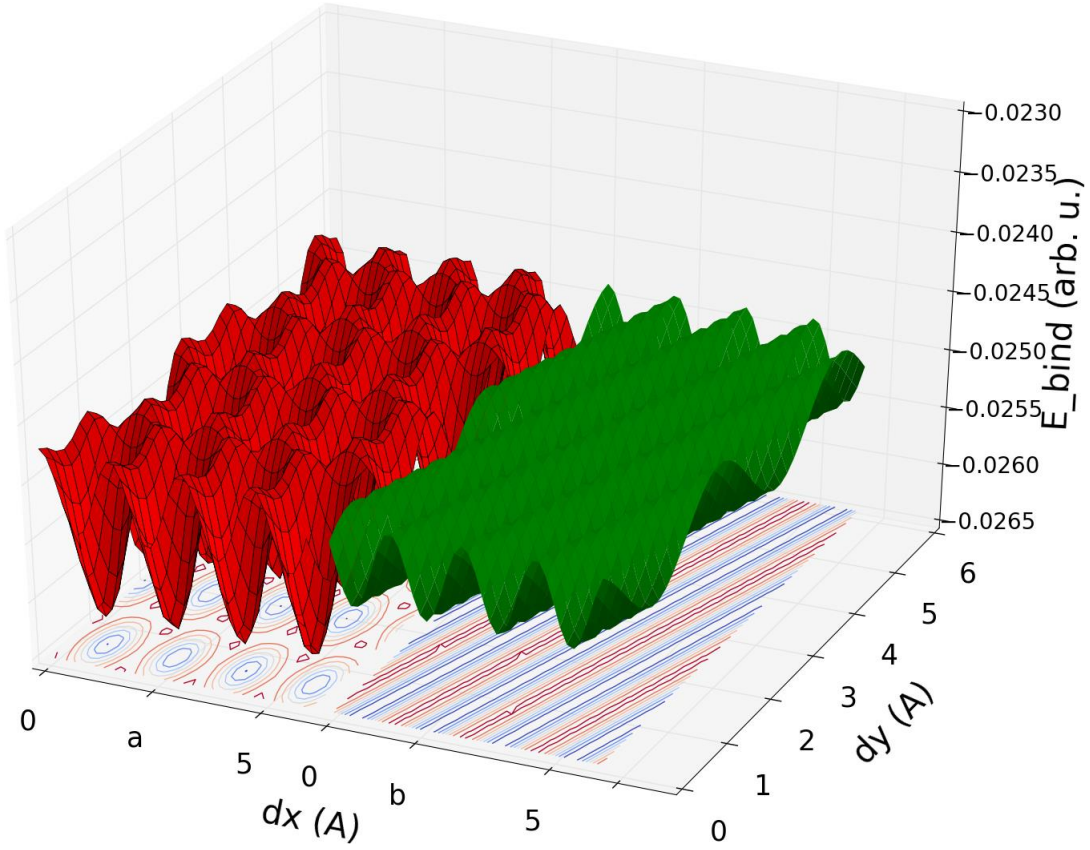

Figure S13. Binding energy as a function of MoS_2 rotation (0 degrees -red, 2 degrees -green) and on the relative x-y shift calculated in the 0-6 Å range in both x and y directions.

From Figure S13, it is obvious that the exact registry determined by the MoS_2 rotation with respect to the surface is crucial for the binding energy achieved through vdW interaction. To realize the special pattern that is characteristic of 0° rotation of the MoS_2, we show two such structures in Figure S14 - one with zero x-y shift and the optimally positioned MoS_2 yielding one of the adsorption minima in Figure S13.

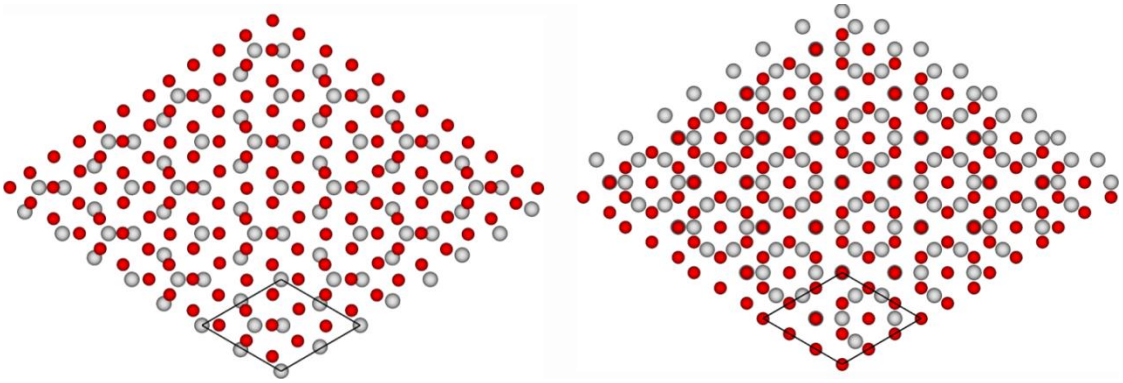

Figure S14. Rotation of 0 degrees with two different x-y shifts. Left - shift (0,0), right - optimal shift yielding the maximum adsorption energy.

Figure S14 reveals the simple mechanism behind preferential orientation and position for the vdW adsorption. Namely, at the optimal configuration almost all sulfur atoms have an identical small distance to either one or 2 top alumina atoms yielding a maximum amount of vdW energy. Such configuration is extremely sensitive to small movement of the MoS_2 structure unlike the other structures - shown in figure S13 (b,c,d) where every sulfur atom has different surroundings of alumina atoms. It is somewhat expected that such structure is less sensitive to exact positions of the MoS_2 layer since the x-y movement simply exchanges surroundings of the sulfur atoms - yielding again similar distribution of surroundings only attributed to different sulfur atoms. More surprising was that such different structures with various rotations of the MoS_2 layer will yield almost exactly the same amount of binding energy.

Finally, we would like to draw a parallel with Lego bricks - portrayed in a figure of the paper which strongly promotes the idea of the vdW heterostructures.[22] Sapphire surface can be seen as a large Lego brick surface while the MoS_2 structure is another one smaller one. One can put MoS_2 onto the surface at any given position and orientation and the gravity (equivalent to vdW force in our model) will keep it bounded to the surface very weakly. One can try attaching it stronger to the surface - but this would require exact arrangement both orientation with respect to the dips as well as the relative shift - so that it snaps in place yielding the strongest possible binding – Figure S15.

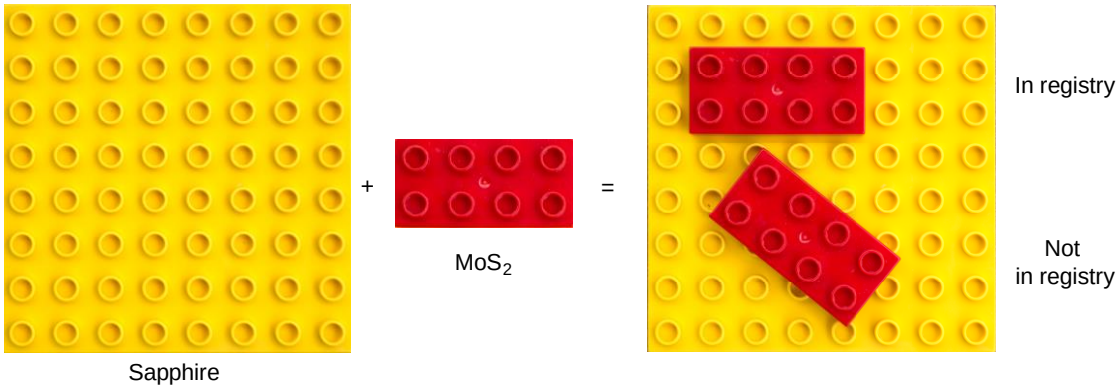

Figure S15. Analogy with Lego bricks. Only the correct orientation and lattice will give rise to an increased interaction between the surface and the overlayer.

5. Electrical transport measurements: single crystals

For electrical transport measurements on single crystals in four-probe geometry, we first transfer CVD-grown single domains of MoS_2 onto a degenerately doped Si substrate covered with 270 nm thick SiO_2 using PMMA A2 as a support film and etching in 30% KOH to detach the polymer film from the sapphire substrate. After transfer, the PMMA film is dissolved in acetone and residues are removed by annealing in Ar atmosphere at 350°C for 5 hours. PMMA A4 was used as the etching mask during oxygen plasma etching, (Figure S16a). We deposit 90 nm thick gold electrodes. The devices are then annealed at 200°C in Ar atmosphere to eliminate resist residues and reduce contact resistance.

In a second annealing step, the devices were annealed in vacuum (5×10^{-7} mbar) for ~15 hours at 130-140°C in order to remove water and other adsorbates from the surface of the 2D semiconducting channel.[23] Electrical measurements were performed immediately after this in vacuum. Figure S16b shows the current vs. bias voltage (I_{ds} vs. V_{ds}) characteristics of our device for several different values of the gate voltage V_g. The observed linear I_{ds}-V_{ds} characteristics indicate the high quality of contacts and the absence of significant charge injection barriers at room temperature. Figure S16c shows the transfer characteristics (I_{ds} vs V_g) of the device from Figure S16a recorded for a bias voltage V_{ds} = 2 V. The source-drain distance is L = 6.7 µm, l_{12} = 4 µm is the distance between the voltage probes V_1 and V_2 and the device width W = 8.3 µm. From this curve, we can obtain the field-effect mobility μ_{FE} defined as $\mu_{FE} = [dG/dV_g] \times [l_{12}/(WC_{ox})]$ where G is the four-probe conductance defined as $G = I_{ds}/(V_1-V_2)$ with I_{ds} the drain current, $V_1 - V_2$ the measured voltage difference between the voltage probes and $C_{ox} = 1.3\times10^{-4}$ F/m^2 the capacitance between the channel and the back gate per unit area. At high gate voltages we observe the mobility reach a value of 43 cm²/Vs, comparable to results from previous two-terminal measurements on CVD MoS_2 (ref. 24) and slightly higher than in several reports on devices based on exfoliated MoS_2.[23, 25] Typical FETs produced using exactly the same fabrication procedure as the CVD material, with the absence of transfer and related possible polymer film contamination, show peak room-temperature mobilities in the 20-30 cm^2/Vs range.

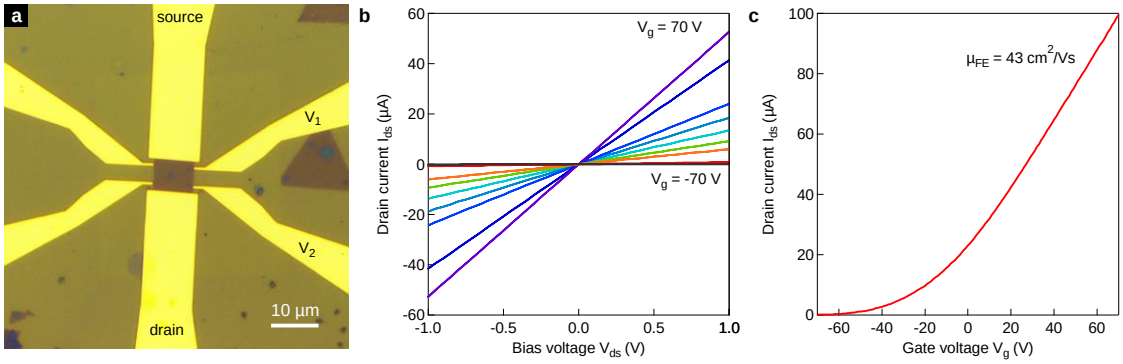

Figure S16. Electrical properties of single-crystal monolayer MoS_2. a, Optical image of a Hall-bar device based on a single-crystal island of MoS_2 transferred onto SiO_2. **b,** Sweeps of current I_{ds} *vs.* bias voltage V_{ds} characteristics of the device shown in a, indicating ohmic-like behavior of the contacts. **c,** Current as a function of gate voltage shows n-type behavior. We extract maximum field-effect mobility μ_{FE} = 43 cm^2/Vs.

6. Scanning Kelvin probe microscopy

In order to study the electrical properties of grain boundaries, new substrates were prepared with the aim of achieving significant doping levels by applying gate voltages in the ±10V range. This range of gate voltages is imposed by the AFM electronics. Metallic local gates consisting of Cr/Au (10/50 nm) were deposited on an intrinsic silicon substrate and covered with a 45 nm thick HfO_2 layer deposited by atomic layer deposition (ALD). CVD MoS_2 was then transferred from the sapphire growth substrate on the HfO_2 substrate with local gates, Figure S17a. Grain boundaries of each type formed by two single domains were then located using optical microscopy and 90 nm Au contacts were defined by electron beam lithography.

For the KPFM measurement a Cypher atomic force microscopy system (Asylum Research) was utilized allowing the simultaneous measurement of topography and local potential with spatial resolution of about 20 nm and a potential resolution of few millivolts. We used silicon KPFM probes (Olympus, OMCL-AC240TM) with a nominal tip radius of ~30 nm, which were covered with a conductive Ti/Pt (5/20 nm) layer and had a resonance frequency of ~70 kHz. An AC modulation voltage V_{AC} of 2 V was applied for the Kelvin probe measurements. An external bias between the two contacts (source and drain) V_{ds} of 1 V was applied and the gate voltage V_g was varied between -6 and +6 V. The electrical current corresponding to V_{ds} was simultaneously recorded using an I/V converter. All measurements were performed under ambient conditions. The schematic drawing of the experimental setup and device geometry is shown on Figure S17a. On Figure S17b, we shown an example of a potential map acquired across two merging islands showing a relative orientation of 94°. Unlike in the cases presented in the main text, such a low-symmetry situation results in a twin grain boundary which manifests itself as an additional potential drop across the channel (Figure S17c), indicating that it introduces extra resistance,[26] equivalent to an additional ~ 4µm long section of MoS_2.

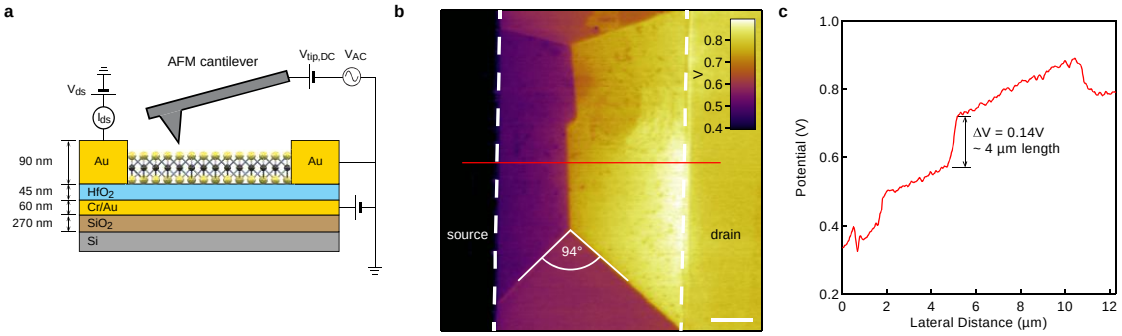

Figure S17. Scanning Kelvin probe imaging of grain boundaries. a, Schematic drawing of the setup and device layout for Kelvin probe imaging. **b,** Example of a potential map and potential profile across a resistive grain boundary formed between two single-crystal grains with a relative orientation angle that does not correspond to the high-symmetry direction of the MoS_2 lattice. Scale bar is 2 μm long. **c,** Potential profile along the red line in b. The presence of a tilt grain boundary introduces additional voltage drop and resistance, equivalent to an additional section of MoS_2 with a length of 4μm.

7. Electrical transport measurements: large-area films

Just like in the case of FETs based on single-crystal CVD MoS_2, the fabrication of large-area devices begins with the transfer procedure which has been optimized for transferring large-area films. Sapphire chips were first spin coated with PMMA 950 MW 2% in anisole at 1500 rpm for 60s and left in vacuum in a desiccator for 12 hours in order to remove the solvent from the resist. The resist was not baked in order to avoid possible build-up of mechanical stress. Films were detached in KOH (30%) at moderate temperatures (60-70 °C), washed in DI water and transferred on Si/SiO_2 chips, drying at 40 °C for 40 minutes. The resist was removed by dipping the sample in acetone for 12 hours, followed by rinsing with isopropanol and drying in N_2, followed by annealing in low vacuum (10^{-2} mbar) for 5h at 350 °C in the flow of argon gas. This resulted in clean and intact films with large regions applicable for device fabrication and minimal damage caused by transfer process.

Prior to measurements, the devices are annealed in vacuum (5×10^{-7} mbar) for ~50 hours at 130-140°C in order to remove water and other adsorbates from the surface of the 2D semiconducting channel[23]. The transfer characteristics (I_{ds} vs V_g) of the device recorded for a bias voltage V_{ds} = 1 V is shown on Figure S18a for different combinations of leads, as labeled in the inset of Figure 6 in the main manuscript. We can use two distinct configurations of leads: nearest neighbors, in which two neighboring leads are used as source and drain electrodes and other combinations allowing us to probe the full length of the device (~ 80 μm) where the region between the source electrodes can contain multiple leads that are disconnected during the measurements. Such leads could be considered to represent invasive contacts and introduce additional scattering because of a local change in the chemical potential induced by the presence of a metal with a different work function than that of the semiconducting channel. This implies that mobilities obtained using such lead combinations could in fact be underestimated.

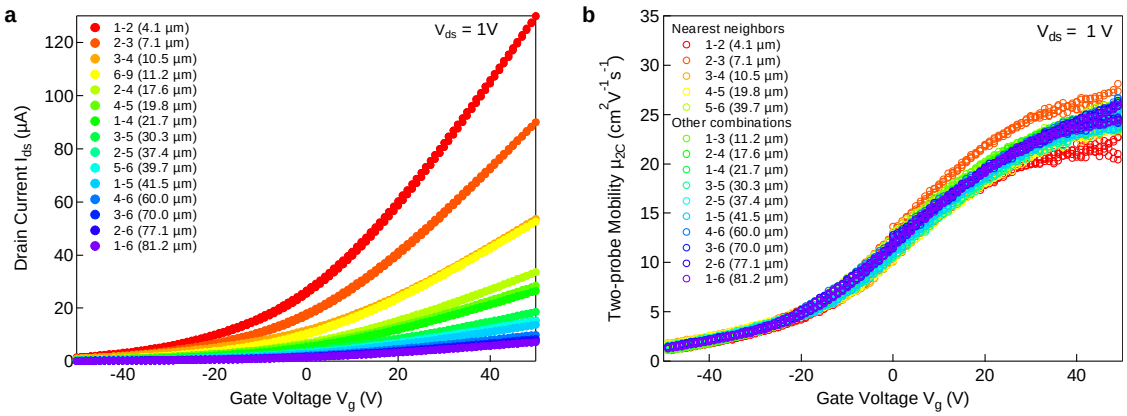

Figure S18. Electrical properties of large-area monolayer MoS_2. a, Drain current I_{ds} as a function of gate voltage recorded for different combinations of electrodes shown in the main Figure 6. **b,** Two-contact field-effect mobility extracted from the transconductance $g_m = dI_{ds}/dV_g$ obtained by differentiating the curves in a.

By differentiating the transfer curves with respect to the gate voltage, we obtain the two-contact effective field-effect mobility μ_{2C} defined as $\mu_{2C} = [dI/dV_g] \times [L/(W \cdot C_{ox} \cdot V_{ds})]$ where I_{ds} is the drain current, L the channel length, W its width, V_{ds} the bias voltage and $C_{ox} = 1.3\times10^{-4}$ F/m^2 the capacitance between the channel and the back gate per unit area. Because the contact resistance is neglected (equivalent to assuming that the bias voltage V_{ds} corresponds to the entire voltage drop over the semiconducting channel), the obtained mobility values are underestimated. The obtained mobility values as a function of gate voltage are shown on Figure S18b and fall within the 20-27 cm^2/Vs range at V_g = 45V irrespective of the channel length or the combination of leads used (nearest neighbors or other).

The devices fabricated on continuous films are expected to contain numerous grains and were located without knowledge of the relative orientation of grains within the channel. We estimate the average triangle size for the CVD material based on which we fabricated the devices to be approximately 10 μm. We then estimate the lower bound for the defect density in the channel of our large-area transistors.

We consider the simplest case, where the triangles of the same size are regularly spaced and form 60° grain boundaries. This is schematically depicted on Figure S19 where triangles merge and form a continuous film, a segment of which is presented in the form of a big triangle, containing several grains. First, we position our transistor channel parallel to the long edge of triangles (blue transparent rectangle on Figure S19). Each triangle forms two grain boundaries with the neighbors along the current path. Based on a typical triangle edge length of 10 μm, we reach a lower estimate of a possible linear defect density to be 0.2 μm^{-1}. We notice that tilting the channel to the triangle edge will provide more grain boundaries. For example, a 90° tilt will result in an increased number of boundaries per unit length (green rectangle in Figure S19). More complicated cases, where the distance between the growth centers is smaller than that considered in our simple model and where 90° boundaries are taken into account, provide the increase of linear grain boundary density. We also notice that in reality, grain positioning will be much more complex. Based on this, we expect for a total length of 82 μm (device in the inset of Figure 6 in the main manuscript) at least 16 grain boundaries along the current path.

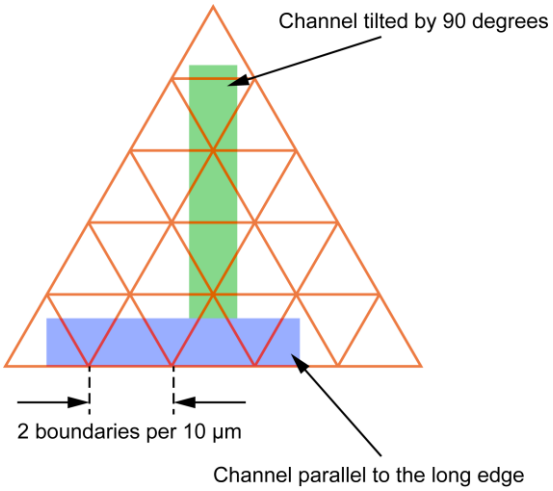

Figure S19. Schematic of channel location inside the continuous film. Schematic of the orientation of the transistor channel with respect to grains inside the continuous film.

References

1. Brivio, J.; Alexander, D. T. L.; Kis, A. Ripples and Layers in Ultrathin MoS_2 Membranes. Nano Lett. 2011, 11, 5148-5153.
2. van der Zande, A. M.; Huang, P. Y.; Chenet, D. a.; Berkelbach, T. C.; You, Y.; Lee, G.-H.; Heinz, T. F.; Reichman, D. R.; Muller, D. A.; Hone, J. C. Grains and Grain Boundaries in Highly Crystalline Monolayer Molybdenum Disulphide. Nat. Mater. 2013, 12, 554-561.
3. Wood, E. A. Vocabulary of Surface Crystallography. J. Appl. Phys. 1964, 35, 1306-1312.
4. Paolo, G.; Stefano, B.; Nicola, B.; Matteo, C.; Roberto, C.; Carlo, C.; Davide, C.; Guido, L. C.; Matteo, C.; Ismaila, D., *et al*. Quantum Espresso: A Modular and Open-Source Software Project for Quantum Simulations of Materials. J. Phys.: Condens. Matter 2009, 21, 395502.
5. Sabatini, R.; Gorni, T.; de Gironcoli, S. Nonlocal Van Der Waals Density Functional Made Simple and Efficient. Physical Review B 2013, 87, 041108.
6. Vydrov, O. A.; Van Voorhis, T. Nonlocal Van Der Waals Density Functional: The Simpler the Better. The Journal of Chemical Physics 2010, 133, 244103
7. Blöchl, P. E. Projector Augmented-Wave Method. Physical Review B 1994, 50, 17953-17979.
8. Kresse, G.; Joubert, D. From Ultrasoft Pseudopotentials to the Projector Augmented-Wave Method. Physical Review B 1999, 59, 1758-1775.
9. Kresse, G.; Furthmüller, J. Efficient Iterative Schemes for *Ab Initio* Total-Energy Calculations Using a Plane-Wave Basis Set. Physical Review B 1996, 54, 11169-11186.
10. Kresse, G.; Hafner, J. *Ab Initio* Molecular Dynamics for Liquid Metals. Physical Review B 1993, 47, 558-561.
11. Dion, M.; Rydberg, H.; Schröder, E.; Langreth, D. C.; Lundqvist, B. I. Van Der Waals Density Functional for General Geometries. Phys. Rev. Lett. 2004, 92, 246401.
12. Klimeš, J.; Bowler, D. R.; Michaelides, A. Chemical Accuracy for the Van Der Waals Density Functional. J. Phys.: Condens. Matter 2010, 22, 022201.
13. Klimeš, J.; Bowler, D. R.; Michaelides, A. Van Der Waals Density Functionals Applied to Solids. Physical Review B 2011, 83, 195131.
14. Caciuc, V.; Atodiresei, N.; Callsen, M.; Lazić, P.; Blügel, S. *Ab Initio* and Semi-Empirical Van Der Waals Study of Graphene–Boron Nitride Interaction from a Molecular Point of View. J. Phys.: Condens. Matter 2012, 24, 424214.
15. Hyldgaard, P.; Berland, K.; Schröder, E. Interpretation of Van Der Waal Density Functionals. ArXiv 2014, 1408.2075.
16. Lazić, P.; Atodiresei, N.; Alaei, M.; Caciuc, V.; Blügel, S.; Brako, R. Junolo – Jülich Nonlocal Code for Parallel Post-Processing Evaluation of Vdw-Df Correlation Energy. Comput. Phys. Commun. 2010, 181, 371-379.
17. Busse, C.; Lazić, P.; Djemour, R.; Coraux, J.; Gerber, T.; Atodiresei, N.; Caciuc, V.; Brako, R.; N'Diaye, A. T.; Blügel, S., *et al*. Graphene on Ir(111): Physisorption with Chemical Modulation. Phys. Rev. Lett. 2011, 107, 036101.

18. Mittendorfer, F.; Garhofer, A.; Redinger, J.; Klimeš, J.; Harl, J.; Kresse, G. Graphene on Ni(111): Strong Interaction and Weak Adsorption. Physical Review B 2011, 84, 201401.
19. Berland, K.; Hyldgaard, P. Analysis of Van Der Waals Density Functional Components: Binding and Corrugation of Benzene and C60 on Boron Nitride and Graphene. Physical Review B 2013, 87, 205421.
20. Runte, S.; Lazić, P.; Vo-Van, C.; Coraux, J.; Zegenhagen, J.; Busse, C. Graphene Buckles under Stress: An X-Ray Standing Wave and Scanning Tunneling Microscopy Study. Physical Review B 2014, 89, 155427.
21. Grimme, S. Semiempirical Gga-Type Density Functional Constructed with a Long-Range Dispersion Correction. J. Comput. Chem. 2006, 27, 1787-1799.
22. Geim, A. K.; Grigorieva, I. V. Van Der Waals Heterostructures. Nature 2013, 499, 419-425.
23. Baugher, B.; Churchill, H. O. H.; Yang, Y.; Jarillo-Herrero, P. Intrinsic Electronic Transport Properties of High Quality Monolayer and Bilayer MoS_2. Nano Lett. 2013, 13, 4212-4216.
24. Schmidt, H.; Wang, S.; Chu, L.; Toh, M.; Kumar, R.; Zhao, W.; Castro Neto, A. H.; Martin, J.; Adam, S.; Özyilmaz, B., *et al*. Transport Properties of Monolayer MoS_2 Grown by Chemical Vapor Deposition. Nano Lett. 2014, 14, 1909-1913.
25. Radisavljevic, B.; Kis, A. Mobility Engineering and a Metal-Insulator Transition in Monolayer MoS_2. Nat. Mater. 2013, 12, 815-820.
26. Najmaei, S.; Amani, M.; Chin, M. L.; Liu, Z.; Birdwell, A. G.; O'Regan, T. P.; Ajayan, P. M.; Dubey, M.; Lou, J. Electrical Transport Properties of Polycrystalline Monolayer Molybdenum Disulfide. ACS Nano 2014, 8, 7930-7937.